Visual Perception-Based Fault Diagnosis in Froth Flotation Using Statistical Approaches

Jin Zhang, Zhaohui Tang*, Yongfang Xie, Mingxi Ai, and Weihua Gui

Abstract: Froth flotation is an important mineral concentration technique. Faulty conditions in flotation processes may cause the huge waste of mineral resources and reagents, and consequently, may lead to deterioration in terms of benefits of flotation plants. In this paper, we propose a computer vision-aided fault detection and diagnosis approach for froth flotation. Specifically, a joint Gabor texture feature based on the Copula model is designed to describe froth images; a rejection sampling technique is developed to generate training sets from the quality distribution of real flotation products, and then an isolation forest-based fault detector is learned; and a fault diagnosis model based on spline regression is developed for root cause identification. Simulation experiments conducted on the historical industry data show that the proposed strategy has better performance than the alternative methods. Thereafter, the entire framework has been tested on a lead-zinc flotation plant in China. Experimental results have demonstrated the effectiveness of the proposed method.

Key words: fault diagnosis; Gabor; copula model; isolation forest; rejection sampling

1 Introduction

Fault detection and diagnosis are important and challenging problems in many disciplines, such as hot strip mill rolling[1], bearing in rotary machinery systems[2,3], minerals processing[4], and wireless sensor networks[5]. According to Ref. [6], a fault in a process is defined as a deviation of an observed output or operating variable from an acceptable range. In the present paper, a case in point is the froth flotation, which is extensively used in the processing of mineral ore deposits as a method of separating the desired mineral components from their associated gangue materials. In the flotation industry, two extreme conditions are viewed as abnormal process behaviors. The first one is related to a situation when froth is overloaded with mineral particles (hereinafter, denoted as Fault 1). The other one is observed when several mineral particles are covered on a bubble surface (denoted as Fault 2). These two flotation conditions may cause large losses of time and reagents to rectify the fault and reduce production efficiency due to the waste of raw materials. If a fault can be quickly detected and identified, appropriate controls can be applied in a timely manner. Therefore, a well-designed fault analysis approach can improve efficiency and save costs[7]. To accomplish this kind of work, the authors in Ref. [8] introduced a non-parametric kernel estimator to approximate the Probability Distribution Function (PDF) of a bubble size after the froth image segmentation, and then a dynamic weight model for bubble size PDF was built. Based on this model, the Lyapunov stability condition was considered to perform the fault detection. In Ref. [9], an equivalent bubble size feature was designed by calculating the white area of each binary image after applying the wavelet transform and reconstruction, and the flotation fault detection was performed by determining the range of a normal froth image. In Ref. [10], the authors proposed to use kernel machines to extract nonlinear features from froth images,

- Jin Zhang, Zhaohui Tang, Yongfang Xie, Mingxi Ai, and Weihua Gui are with the School of Automation, Central South University, Changsha 411083, China. E-mail: zhang_jin@csu.edu.cn; zhtang@csu.edu.cn; yfxie@csu.edu.cn; mingxi_ai@csu.edu.cn; gwh@csu.edu.cn.
- * To whom correspondence should be addressed.

and a one-class support vector machine was used to define a confidence region for normal instances based on the extracted features. Instances outside the confidence region were considered as faults.

As shown in Fig. 1, the froth surface appearances of the two kinds of faults are extremely different. An individual bubble can be easily identified in the case of Fault 2, whereas it is impossible to segment a froth image of Fault 1 into individual bubbles. An image feature based on the size of a bubble is not able to distinguish Fault 1 from the normal working conditions. Moreover, in the case of binary transform, it is difficult to obtain discriminative descriptions for Fault 2 and normal instances. The Gabor functions[11, 12], in which kernels are similar to responses of two-dimensional receptive field profiles of a mammalian simple cortical cell, have been demonstrated a great success being applied to the bauxite flotation working condition recognition[13]. In the present study, we attempt to apply the Gabor transform to the fault detection and diagnosis task. Generally, the Gabor texture is represented by a distribution of magnitude (Magnitude-based Gabor Texture Representation (MGTR)) and a phase (Phase-based Gabor Texture Representation (PGTR))[14, 15]. However, when applying PGTR to the froth texture representation, we find that it is not possible to describe froth images, as demonstrated in Fig. 2. To mitigate this deficiency, we propose to replace PGTR with the Real part of the Gabor Texture Response (RGTR) and the Imaginary part of the Gabor Texture Response (IGTR). However, in Ref. [13], the interscale and intrascale statistical dependencies across MGTR, RGTR, and IGTR were neglected due to the univariate density modeling approach. To provide a complete statistical description for the Gabor texture, we construct a joint model including MGTR, RGTR, and IGTR based on the multivariate Copula approach[16–18].

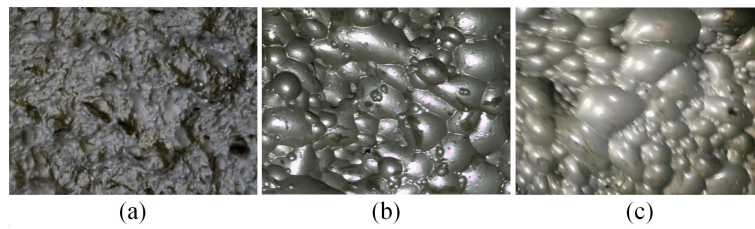Generally, the model-based approaches require a

Fig. 1   Illustration of froth flotation working conditions: (a) Fault 1-froths were heavily loaded with minerals; (b) normal working condition; and (c) Fault 2-froths contained the small amount of gangue minerals.
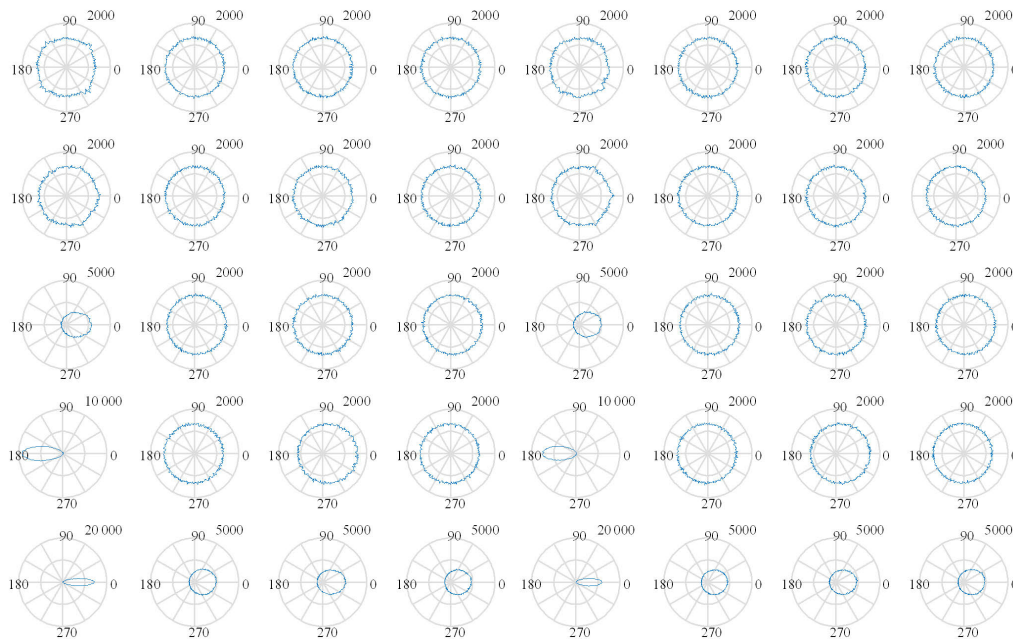

Fig. 2   Polar plots of the phase part of the Gabor froth textures in five scales and eight orientations. There is almost no obvious orientation specificity in the phase of Gabor responses.

priori mathematical knowledge of the process. However, the dynamic behavior of the flotation process is difficult to understand. Therefore, it is a challenging task to build a dynamic weight model for bubble size PDF. In turn, the data-driven schemes serve as an efficient alternative way, which only depends on the measured process variables[19, 20]. A general structure of computer vision-aided fault detection and diagnosis method implies defining an image feature extraction model together with a classifier methodology[21, 22]. In the flotation industry, the property and grade of raw ore are two primary disturbances that cause serious deviation in the flotation working conditions. At the same time, the fluctuation magnitude of the property and grade of raw ore is small. Even though it is possible to collect a large number of production data in a day, the number of working condition types is very small. Therefore, it is difficult to learn a robust fault classifier based on the industry data collected in a short period of time. Instead of training a classifier, in this study, we propose to build an isolation forest model (iForest) considering that it is well applicable to the cases with the insufficient amount of fault training data[23]. In iForest, faulty conditions are detected as the instances that have short average path lengths on the isolation trees (iTrees). Therefore, it is important to construct a training set that has a prevailing majority of normal instances and only a small number of fault instances. From the mathematical point of view, flotation conditions are random variables that obey stochastic distribution, and the probability of fault conditions in this distribution is small. Based on these observations, in this study, we propose to generate training sets from the real distribution of the flotation working conditions.

Once a fault is successfully detected, the root cause should be identified as soon as possible. As the flotation process mechanics are still difficult to understand, it is almost impossible to diagnose flotation faults based on the kinetic mechanisms. From the data-driven perspective, if we have the root cause label for each fault instance and obtain a considerable number of real fault instances, a data-driven based fault diagnosis model can be trained on the labeled historical data[19, 24]. However, in real application, it is difficult to collect a large number of fault instances with a manual root cause label. In this setting, a Thin-Plate Spline Regression (TPSR)[25, 26] model is developed to learn the relationship between a fault root cause (e.g., a manipulation variable, such as a foaming agent and an activator) and a product visual

appearance.

Therefore, contributions of the present paper are as follows:

● The Gabor texture feature based on a Copula model is designed to describe the froth surface appearance.

● To detect flotation faults using an isolation forest approach, a rejection sampling technique is developed to generate training sets from the distribution of the real flotation working conditions.

● A flotation fault diagnosis model based on spline regression is developed and confirmed to perform well in the cases when only a small number of training sets are available.

2　Description of Froth Flotation

Froth flotation is a vital mineral concentration process. It takes advantage of hydrophobicity of liberated minerals and separates these minerals one from another and from slurry they are in. Specifically, in the flotation process, the ore is firstly ground to a size sufficient to liberate desired minerals from the gangue, and then liberated minerals are conditioned as slurry by using moderate reagents, which make their surfaces hydrophobic and provide them with the tendency to get attached to air bubbles. After that, the conditioned mineral slurry is projected to flotation banks. A schematic of a flotation bank is shown in Fig. 3. During stirring of an agitator, hydrophobic minerals get attached to the air bubbles and float to the top of the flotation bank, thereby forming a froth layer. The froth is skimmed off as a product of this bank. The remaining unfloated particles are discharged as tailings. As the morphologic structure of froth is largely influenced by mineral particles attached to air bubbles, in industry, the visual appearance of the froth layer serves as an indicator of the flotation performance. Furthermore, chemical reagents can be changed when observing the froth surface. Let us consider an example of zinc froth flotation concentrator in Shaoguan, China.
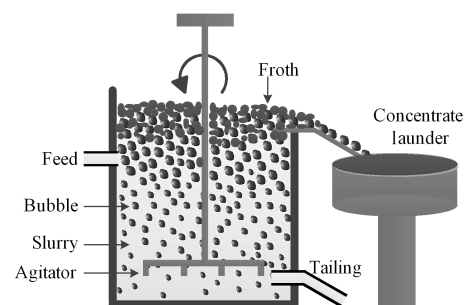

Fig. 3　Schematic of flotation bank.

To achieve the designed metallurgical performance, the parameters of a foaming agent (used to stabilize foams), an activator (attaches itself to the surface of minerals to facilitate other reagents reacting to it), and a collector (used to change the mineral surface hydrophobicity) need to be carefully controlled. Within this plant, if the concentrate grade is smaller than 52%, the flotation condition will be recognized as Fault 2. If the concentrate grade is larger than 56%, it will be recognized as Fault 1. Root causes and the corresponding fault type are summarized in Table 1.

If the amount of the injected foaming agent is superfluous, the flotation bank will produce excessive bubbles, and thereby, this may lead to Fault 2 (a small number of mineral particles are covered on the froth layer). On the contrary, if the amount of the injected foaming agent is insufficient, the number of bubbles to support mineral particles is too small as well, and thereby, this may cause Fault 1 (froth is overloaded with mineral particles). If the amount of the injected collector/activator is excessive, not only fine particles can get attached to air bubbles, but also coarse particles may get attached to bubbles. Consequently, Fault 1 occurs. However, if the insufficient amount of the collector/activator is injected, only a small portion of fine particles will get attached to air bubbles, causing Fault 2. To achieve the accurate fault detection and diagnosis, the industrial field data were collected for a period of approximately three months at a sampling interval of 20 min. There were 6335 concentrate grade records collected. Histogram distribution of the concentrate grade data is summarized in Fig. 4. The ratio of the normal concentrate grade in the collected data is 0.8524, the ratio of Fault 1 is 0.0955, and the ratio of Fault 2 is 0.0521.

3 Feature Extraction Using Statistical Method

3.1 Gabor wavelet texture

In the spatial domain, a two-dimensional Gabor filter

Table 1 Froth flotation faults and three kinds of root causes. "+" means that the corresponding reagent is excessive and "–" means that the corresponding reagent is insufficient.

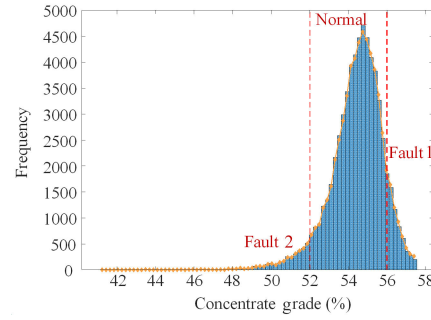| Fault	Root cause		
	Foaming agent	Activator	Collector
Fault 1 (concentrate grade>56%)	–	+	+
Fault 2 (concentrate grade<52%)	+	–	–

Fig. 4 Histogram distribution of the concentrate grade data.

is a Gaussian kernel function modulated by a complex sinusoidal plane wave defined as follows:

$$\begin{cases} G(x, y) = \dfrac{f^2}{\pi\gamma\eta}\exp\left(-\dfrac{x'^2+\gamma^2 y'^2}{2\sigma^2}\right)\exp(i2\pi f x'+\phi), \\ x' = x\cos\theta + y\sin\theta, \\ y' = -x\sin\theta + y\cos\theta \end{cases}$$

(1)

where $i = \sqrt{-1}, \eta = \dfrac{1}{2}, f$ is the frequency of the sinusoidal factor, θ represents the orientation of the normal strips to the parallel ones of the Gabor function, ϕ is the phase offset, σ is the standard deviation of the Gaussian envelope, and γ is the spatial aspect ratio, which specifies the ellipticity of the support of the Gabor function. Forty Gabor filters in five scales and eight orientations are considered in the present study. The Gabor representation of a froth image can be obtained by convolving the image with Gabor kernels. Let $I(x, y)$ be the gray-level froth image, then the convolution of the image and a Gabor kernel $G(x, y)$ are defined as follows:

$$O_{s, d}(x, y) = I(x, y) \times G_{s, d}(x, y) \quad (2)$$

where $s = 0, \ldots, 4$ and $d = 0, \ldots, 7$ denote scales and directions of the Gabor kernels, respectively. The output $O_{s, d}(x, y)$ is a complex. Usually, the Gabor texture information are captured from the magnitude and phase parts[14]:

$$M_{s,d}(x, y) = \sqrt{\left(\mathrm{Re}\left(O_{s,d}(x, y)\right)\right)^2 + \left(\mathrm{Im}\left(O_{s,d}(x, y)\right)\right)^2} \quad (3)$$

$$P_{s,d}(x, y) = \tan^{-1}\left(\dfrac{\mathrm{Im}\left(O_{s,d}(x, y)\right)}{\mathrm{Re}\left(O_{s,d}(x, y)\right)}\right),$$
$$-\pi < P_{s,d}(x, y) < \pi \quad (4)$$

where $\mathrm{Re}\left(O_{s,d}(x, y)\right)$ and $\mathrm{Im}\left(O_{s,d}(x, y)\right)$ mean the real part and the imaginary part of $O_{s,d}(x, y)$, respectively.

The Gamma distribution (Γ_{D}) is introduced to model the magnitude part of the Gabor wavelet transform in

which the PDF can be expressed as follows[13–15,27]:

$$
\begin{cases}
f(x;\alpha,\beta) = \dfrac{\alpha^{\beta}}{\Gamma(\beta)} x^{\beta-1} e^{-\alpha x}, \ x \geqslant 0; \\
\Gamma(z) = \displaystyle\int_{0}^{\infty} x^{z-1} e^{-x} \mathrm{d}x, \ z \geqslant 0
\end{cases}
\tag{5}
$$

where α is the scale parameter, which controls the width of the PDF peak and β is the shape parameter, which is inversely proportional to the decreasing rate of the peak. The two parameters can be estimated by the maximum likelihood estimation method. Let $X = \{x_1, x_2, \ldots, x_n\}$ be a random sample with the assumption that the data are mutually independent. Then the log-likelihood function is defined as follows:

$$
L(x;\alpha,\beta) = \ln\left(\prod_{i=1}^{n} f(x_i;\alpha,\beta)\right)
\tag{6}
$$

By differentiating the log-likelihood function with respect to α and β and setting them to zero, the parameters satisfy the following condition:

$$
y = \ln(\beta) - \psi(\beta)
\tag{7}
$$

$$
\overline{x} = \frac{\beta}{\alpha}
\tag{8}
$$

where $y = \ln(\overline{x}/\widehat{x})$, $\overline{x} = \dfrac{1}{n}\sum_{i=1}^{n} x_i$ is the arithmetic mean of the sample data, $\widehat{x} = \left(\prod_{i=1}^{n} x_i\right)^{1/n}$ is the geometric mean of sample data, and $\psi(z) = \Gamma'(z)/\Gamma(z)$ is the digamma function. Therefore, an iteration scheme for β can be obtained as follows:

$$
\widehat{\beta}_k = \frac{\widehat{\beta}_{k-1}\left(\ln\left(\widehat{\beta}_{k-1}\right) - \psi\left(\widehat{\beta}_{k-1}\right)\right)}{y}
\tag{9}
$$

After obtaining the estimate of $\widehat{\beta}$, $\widehat{\alpha}$ can be derived directly by using Eq. (8). As MGTR statistically follows the gamma distribution, the texture information from the Gabor magnitude can be characterized using model parameters $\left(\widehat{\alpha}, \widehat{\beta}\right)$ as follows:

$$
\mathrm{MGTR} = \Big[\left(\widehat{\alpha}(s,d), \widehat{\beta}(s,d)\right) :
$$
$$
s = 0, \ldots, 4; d = 0, \ldots, 7\Big]
\tag{10}
$$

To model the real and the imaginary parts of the Gabor texture response (RGTR and IGTR, respectively), the t location-scale distribution is utilized. PDF of the two-parameter t location-scale distribution is defined as follows:

$$
f(x;\mu,v,\omega) = \frac{\Gamma\left(\frac{v+1}{2}\right)}{\omega\sqrt{v\pi}\,\Gamma\left(\frac{v}{2}\right)}\left[\frac{v+\left(\frac{x-\mu}{\omega}\right)^2}{v}\right]^{-\left(\frac{v+1}{2}\right)}
\tag{11}
$$

where μ is the location parameter and ω is the scale parameter. Here, v controls the shape of the distribution (kurtosis). Given μ, v, and ω, a typical student t distribution is then exhibited with v degrees of freedom. The corresponding log-likelihood function can be written as follows:

$$
\zeta(X|\mu,v,\omega) = \ln L(X;\mu,v,\omega) =
$$
$$
\sum_{i=1}^{n}\cdot\left\{\ln\frac{\Gamma\left(\frac{v+1}{2}\right)}{\omega\sqrt{\pi v}\,\Gamma\left(\frac{v}{2}\right)} - \frac{v+1}{2}\ln\left[\frac{v+\left(\frac{x_i-\mu}{\omega}\right)^2}{v}\right]^{-\frac{v+1}{2}}\right\} =
$$
$$
n\ln\Gamma\left(\frac{v+1}{2}\right) - n\ln\Gamma\left(\frac{v}{2}\right) + \frac{v}{2}n\ln v - n\ln\omega -
$$
$$
n\ln\pi - \frac{v+1}{2}\sum_{i=1}^{n}\ln\left[v+\left(\frac{x_i-\mu}{\omega}\right)^2\right]
\tag{12}
$$

The maximum likelihood estimation approach can be used to determine the value of $(\widehat{\mu}, \widehat{v}, \widehat{\omega})$. Therefore,

$$
(\widehat{\mu}, \widehat{v}, \widehat{\omega}) = \underset{(\mu,v,\omega)}{\arg\max}\{\zeta(X|\mu,v,\omega)\}
\tag{13}
$$

Equation (13) is not a close-form solution. An iterative procedure is performed to numerically manage the search of the maximum value of the log-likelihood function. Details can be found in our previous work[13]. As RGTR and IGTR statistically follow the t location-scale distribution, the texture information obtained from the real part and the imaginary part can be described using $(\widehat{\mu}, \widehat{v}, \widehat{\omega})$:

$$
\mathrm{RGTR} = \left[(\widehat{\mu}, \widehat{v}, \widehat{\omega})_{(s,d)} : s = 0, \ldots, 4; d = 0, \ldots, 7\right]
\tag{14}
$$

$$
\mathrm{IGTR} = \left[(\widehat{\mu}, \widehat{v}, \widehat{\omega})_{(s,d)} : s = 0, \ldots, 4; d = 0, \ldots, 7\right]
\tag{15}
$$

3.2 Copula model for texture representation

A copula is a B-dimensional distribution function $C : [0,1]^{B} \to [0,1]$ with uniform marginals satisfying certain regularity conditions. The results in Ref. [28] showed that given a B-dimensional random vector with a Cumulative Distribution Function (CDF) $H(x_1, \ldots, x_B)$ and continuous marginal CDFs $F_1(x_1), \ldots, F_n(x_B)$, there exists a B-dimensional copula C such that:

$$
H(x_1, \ldots, x_B) = C(F_1(x_1), \ldots, F_B(x_B))
\tag{16}
$$

This theorem represents the fact that every random variable can be transformed into a uniform one by applying the probability integral transform. In other words, a copula can be considered as a distribution function of marginal CDFs. Moreover, if the function C is continuous and differentiable, then the copula density is given as follows:

$$c(x_1, \ldots, x_B) = \frac{\partial^B C(x_1, \ldots, x_B)}{\partial x_1 \ldots \partial x_B} \quad (17)$$

In this case, the joint PDF of x can be written as follows:

$$f(x_1, \ldots, x_B) = c(F_1(x_1), \ldots, F_B(x_B)) \prod_{i=1}^{B} f_i(x_i) \quad (18)$$

where $f_i(\cdot)$ $(i = 1, \ldots, B)$ are the marginal PDFs. Thereby, a joint multivariate PDF is uniquely defined given marginal PDFs and the copula density.

Several common-used copulas include the Gaussian copula, t-copula, and Archimedean copulas. It has been widely accepted that the Gaussian copula and t-copula can finely fit the sub-bands of the wavelet-based transform[29]. In the present study, the following Gaussian copula is used, as it can be easily implemented, and its dependence structure is intuitive based on correlation coefficients:

$$c(x; \Sigma) = \frac{1}{|\Sigma|^{\frac{1}{2}}} \exp\left[-\frac{1}{2}\vartheta^{\mathrm{T}}\left(\Sigma^{-1} - I\right)\vartheta\right] \quad (19)$$

where $\vartheta_i = \varphi^{-1}(F_i(x_i))$ and φ represents the CDF of the normalized Gaussian distribution $N(0, 1)$. The matrix I is the B-dimensional identity matrix and Σ denotes the correlation matrix. From this, we can derive the joint model as follows:

$$f(x; \zeta) = \frac{1}{|\Sigma|^{\frac{1}{2}}} \exp\left[-\frac{1}{2}\vartheta^{\mathrm{T}}\left(\Sigma^{-1} - I\right)\vartheta\right] \prod_{i=1}^{B} f_i(x_i) \quad (20)$$

where $\zeta = (\xi, \Sigma)$ denotes the hyperparameters of the joint model and $\xi = (\xi_1, \ldots, \xi_B)$ represents a set of the marginal parameters.

As shown in Fig. 5, in this study, the copula models corresponding to MGTR, RGTR, and IGTR are constructed and integrated in three ways:

• For each orientation, the interscale statistical dependence of MGTR, RGTR, and IGTR in all scales is investigated.

• For each scale, the intrascale statistical dependence of MGTR, RGTR, and IGTR in all orientations is investigated.

• For each scale and each orientation, the dependence of MGTR, RGTR, and IGTR is investigated.

A simple procedure to estimate the full set of unknown hyperparameters of a copula joint distribution can be summarized as follows:

(1) The Gamma Distribution (GD) is used as the marginal distribution for MGTR and the t location-scale distribution is used as the marginal distribution for RGTR and IGTR.

(2) Parameters of MGTR, RGTR, and IGTR are estimated using the maximum likelihood method. For simplicity, $\widehat{\xi}$ is used to represent the estimated marginal parameters. Specifically, the GD parameters of MGTR in scale s_i and orientation d_j are denoted as $\widehat{\xi} = (\widehat{\alpha}, \widehat{\beta})$, and the t location-scale distribution parameters of RGTR (IGTR) are denoted as $\widehat{\xi} = (\widehat{\mu}, \widehat{v}, \widehat{\omega})$.

(3) The cumulative distributions of MGTR, RGTR, and IGTR are computed.

(4) Each observation x_i is transformed into ϑ_i using $\vartheta_i = \varphi^{-1}(F_i(x_i))$.

(5) Parameter Σ of the joint distribution is estimated by maximizing the following log-likelihood function:

$$\widehat{\Sigma} = \operatorname*{argmax}_{\Sigma} \sum_{i=1}^{n} \log c\left(F_1\left(x_{1i}; \widehat{\xi}_1\right), \ldots,\right.$$
$$\left. F_B\left(x_{Bi}; \widehat{\xi}_B\right); \Sigma\right).$$

(6) The B-dimensional copula joint model can be derived as

$$f(x; \zeta) = \frac{1}{|\Sigma|^{\frac{1}{2}}} \exp\left[-\frac{1}{2}\vartheta^{T}\left(\Sigma^{-1} - I\right)\vartheta\right] \prod_{i=1}^{B} f_i(x_i).$$
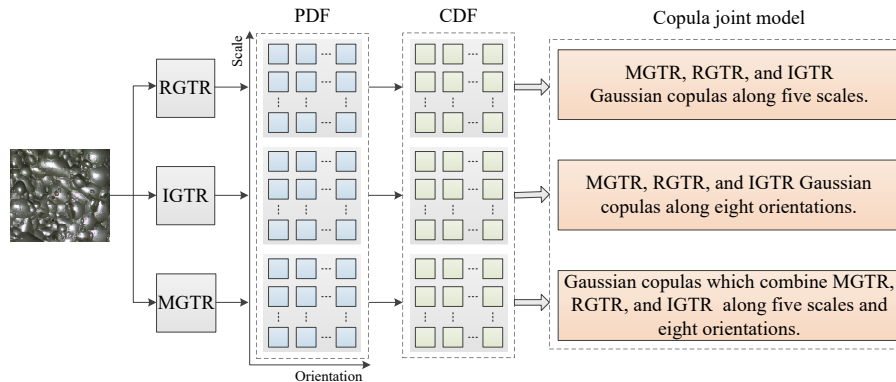

Fig. 5 Copula model for Gabor wavelet texture.

4 Improved Isolation Forest for Fault Detection and Diagnosis

4.1 Isolation forest with Monte Carlo sampling

According to the definition of the iTree approach[23, 30], the node of an isolation tree is either an external node with no child, or an internal node with one test and exactly two daughter nodes (T_l, T_r). A test consists of an attribute q and a split value p, such that the test $q < p$ divides the data points into T_l and T_r. Thereby, an iTree can be built as follows. Given a training set $X = \{x_i\}_{i=1}^{N}$, $x_i \in \mathbb{R}^m$, the instance x_i can be divided recursively by randomly selecting an attribute q and a split value p until any of these conditions holds: (1) the tree reaches a height limit, (2) $|X| = 1$ or (3) all data items in X have the same values. This approach is summarized in Algorithm 1.

As the frequency of fault conditions is low, visual features of these conditions are different from the normal ones, and therefore, they are more susceptible to be isolated. In an iTree, it will produce noticeable shorter paths for faulty conditions comparing with the normal instances. Hence, when a forest of isolation trees (isolation forest) collectively produce shorter path lengths for some particular instances, then these instances are highly likely to be faulty. The anomaly score of an instance is defined as follows[23]:

$$s(x, N) = 2^{-\frac{E(h(x))}{c(N)}} \tag{21}$$

where N is the number of training instances, $h(x)$ is the path length of x, which is measured by the number of edges that x traverses an iTree from the root node to the terminated external node, $E(h(x))$ is the average

---

Algorithm 1. iTree (X, e, l)

Inputs: X–input data, e–current tree height, l–height limit
Output: an iTree
1: **if** $e \geqslant l$ or $|X| \leqslant 1$ **then**
2:     return exNode $\{\text{Size} \leftarrow |X|\}$
3: **else**
4:     let Q be a list of attributes in X
5:     randomly select an attribute $q \in Q$
6:     randomly select a split point p from max and min value of attribute q in X
7:     $X_l \leftarrow \text{filter}(X, q < p)$
8:     $X_r \leftarrow \text{filter}(X, q \geqslant p)$
9:     return inNode $\{\text{Left} \leftarrow \text{iTree}(X_l, e + 1, l)$
10:           Right $\leftarrow \text{iTree}(X_r, e + 1, l)$
11:           SplitAtt $\leftarrow q$
12:           SplitValue $\leftarrow p\}$
13: **end if**

---

of $h(x)$ in a collection of isolation trees, and $c(N)$ is defined as

$$c(N) = 2H(N - 1) - \frac{2(N - 1)}{N} \tag{22}$$

where $H(i)$ is the harmonic number, which can be estimated by $\ln(i) + 0.577\,215\,664\,9$ (the Euler's constant).

As stated in the original work related to the isolation forest method in Ref. [23], training sets should have a prevailing majority of normal instances and a small number of fault instances, as a higher number of fault instances may reduce the ability of iForests to isolate faults from normal instances. Therefore, we propose using the Monte Carlo sampling method to generate training samples for iForest from a concentrate grade probability distribution. Rejection sampling is one of Monte Carlo methods[31]. It is based on the observation that, to sample a random variable, one can sample uniformly from the region under the graph of its density function, specifically, from the probability distribution function $f(x)$. Another distribution function $g(x)$ is defined such that sampling from $g(x)$ becomes an easy task. Then the envelope

$$M = \sup \frac{f(x)}{g(x)} \tag{23}$$

is computed. From Eq. (23), it is seen that $f(x) < M \cdot g(x)$. Thereafter, rejection sampling can be performed as described in Ref. [32]:

- Sample x from $g(x)$ and u from a uniform distribution $U(0, 1)$.
- Check whether $u < f(x)/Mg(x)$ or not.
- If this holds, accept x as a realization of $f(x)$.
- If not, reject the value of x and repeat the sampling step.

Figures 6b–6d show that three training sets were randomly generated using Algorithm 2 (a comprehensive description of rejection sampling). The improved isolation forest using Rejection Sampling (RS-iForest) is described in Algorithm 3. Specifically, 512 samples were generated for each training set. It can be observed that the distribution of these generated training sets is the same as in the database shown in Fig. 6a. It satisfies the condition that the number of faulty instances needs to be small, and the majority of instances are normal.

4.2 Fault diagnosis based on classification

The iForest can distinguish faults from normal working conditions, however, it is not able to differentiate a specific fault type. To recognize whether the current
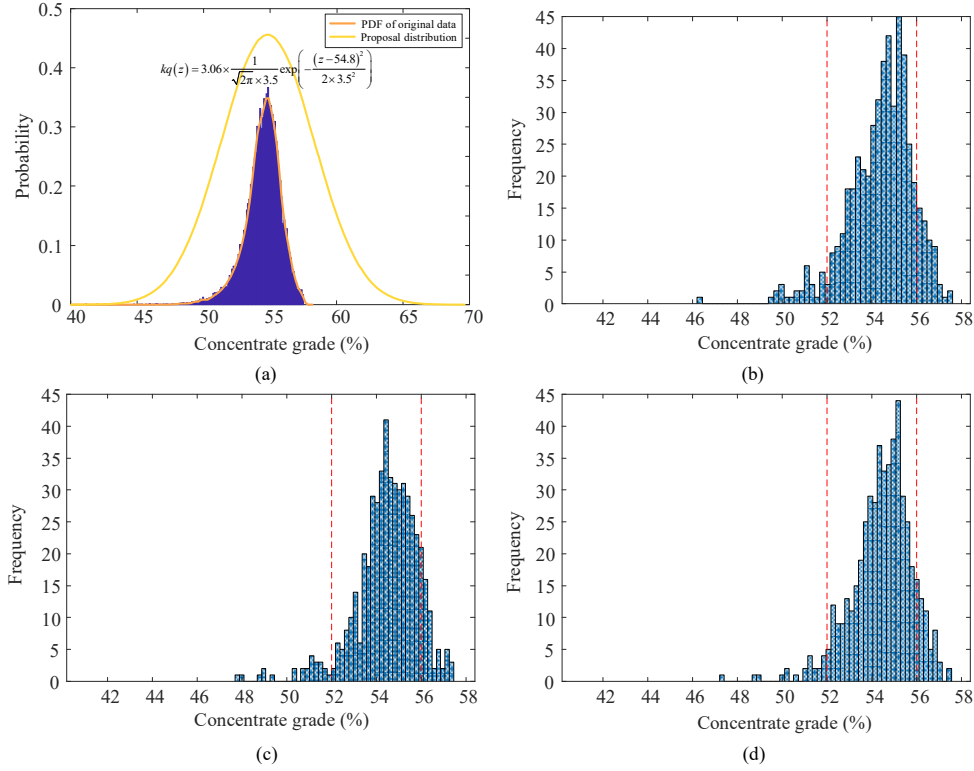
Fig. 6 Generated training sets using the rejection sampling technique. (a) Kernel probability fitting of the grade histogram and the constructed Gaussian proposal distribution. (b)–(d) Results of three random sampling.

Algorithm 2. RejectionSample (X, t, λ)

Inputs: X–input data, t–number of trees, λ–subsampling size
Output: sampled data X'

1: Model the probability distribution of historical concentrate grade X using kernel method

$$f(x) = \frac{1}{Nh} \sum_{i=1}^{n} K\left(\frac{x-x_i}{h}\right)$$

$$K\left(\frac{x-x_i}{h}\right) = \frac{1}{\sqrt{2\pi}} \exp\left(\frac{((x-x_i)/h)^2}{2}\right)$$

2: a normal PDF function $g(x)$ is constructed

$$g(x) = \frac{1}{\sqrt{2\pi}\sigma_{\text{init}}} \exp\left(-\frac{(x-\mu_{\text{init}})^2}{2\sigma_{\text{init}}^2}\right)$$

where μ_{init} and σ_{init} are set by trial-and-error
3: set $M = \max_{x \in X} f(x)/g(x)$
4: **for** $i = 1$ to t do **end if**
5:    **while** size $(X_i') < \lambda$
6:       $x \leftarrow g(x)$
7:       $u \leftarrow U(0, 1)$
8:       **if** $u < f(x)/Mg(x)$
9:          $X_i' \leftarrow X_i' \cup x$
10:      **end if**
11:   **end while**
12: **end for**
13: **return** X'

Algorithm 3. iForest (X, t, λ)

Inputs: X–input data, t–number of trees, λ–subsampling size
Output: a set of t iTrees

1: Initialize Forest
2: set height limit $l = \text{ceiling}(\log_2 \lambda)$
3: $X' \leftarrow$ RejectionSample (X, t, λ)
3: **for** $i = 1$ to t do
4:    Forest $\leftarrow$ Forest $\cup$ iTree $(X_i', 0, l)$
6: **end for**
7: **return** Forest

---

fault belongs to Fault 1 or 2, a Fuzzy C-Means (FCM)[33] clustering method is applied to diagnose a fault type. To identify the root cause for a flotation fault, we need to construct a diagnosis model for each type of fault, as shown in Fig. 7. In general, fault diagnosis methods in an industrial process can be divided into model-based and data-driven ones. Among them, the latter ones that are developed by using the process measurements have drawn more attention over past decades, as the first principle models are rather difficult to be constructed. In the present study, we seek to construct a data-driven based diagnosis model in which the inputs contain the feed condition (e.g., feed grade in froth flotation), manipulation variables (e.g., reagents, such as foaming agent and activator in froth flotation), and the Copula-Gabor texture feature. According to the statistical analysis of the historical data, the probabilities of occurring Faults 1 and 2 are 0.0955 and 0.0521,
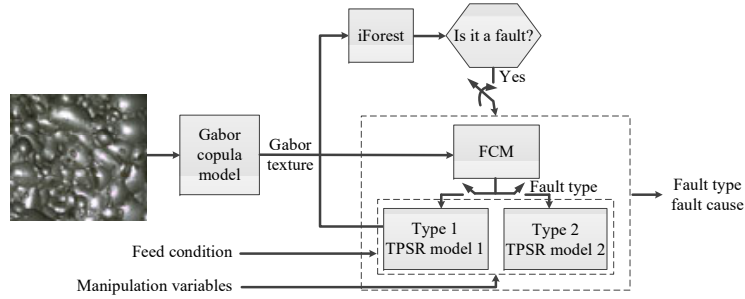
Fig. 7   Illustration of fault diagnosis.

respectively. Therefore, it is difficult to construct a large dataset for training of data-driven models. In this kind of conditions, it is important to develop a data-driven model that requires only a small amount of training data.

The TPSR function constructed from the Sobolev space has demonstrated a great success in terms of semi-supervised learning (a classification task that lacks the sufficient amount of labeled training data)[25, 26, 34]. Let $r \in R$ be the label of the root cause, $x \in R^{d_1}$ be the Copula-Gabor texture feature, $m \in R^{d_2}$ be manipulation variables, and $z \in R^{d_3}$ be the feed grade, so that TPSR attempts to learn a root cause regression model that satisfies the following condition:

$$r \approx \mathcal{G}(x, m, z) = \mathcal{G}(\chi) \tag{24}$$

where $\chi = [x, m, z] \in \Re^{d_1+d_2+d_3}$. This regression task can be solved in a generalized optimization framework with data fitting and function smoothness constraints:

$$\mathcal{G} = \arg\min_{\mathcal{G}} \left\{ \sum_{i=1}^{N} \|r_i - \mathcal{G}(\chi_i)\|^2 + \kappa \cdot \mathcal{S}(\mathcal{G}) \right\} \tag{25}$$

where $\mathcal{S}(\mathcal{G})$ is the smoothness penalty function of $\mathcal{G}$ defined as a semi-norm. There is a unique solution form for Eq. (25) when solving it in the Sobolev space, given as follows:

$$\mathcal{G}(\chi) = \sum_{i=1}^{d} \bar{\omega}_i \, p_i(\chi) + \sum_{j=1}^{N} \tau_j \, \Phi_j(\chi) \tag{26}$$

where $d = (d_1 + d_2 + d_3 + s - 1)! (d_1 + d_2 + d_3)! (s - 1)!$, s is the order of the partial derivative of the semi-norm, $\{p_i(\chi)\}_{i=1}^{d}$ is a set of primitive polynomials that span the polynomial space of total degrees less than s, and $\Phi(\chi)$ is a Green formula. In real applications, the linear polynomial space is used and the Green formula in a radial basis function form is adopted. Therefore, the TPSR function can be calculated as

$$\mathcal{G}(\chi) = \bar{\omega}_0 + \sum_{i=1}^{d_1+d_2+d_3} \bar{\omega}_i \cdot \chi_i + \sum_{j=1}^{N} \tau_j \cdot$$
$$\|\chi - \chi_j\|^2 \cdot \log \|\chi - \chi_j\| \tag{27}$$

where χ_j is the j-th entry of χ. Parameters of $\mathcal{G}(\chi)$ can be learned by substituting Eq. (27) back into Eq. (25) to generate a group of linear equations as stated in Ref. [25].

5   Experiment and Result

5.1   Flotation fault detection

Firstly, we examine the impact of the sub-sampling size on the fault detection performance. The results provide an insight with regard to optimality of the sub-sampling. In this experiment, we consider several different sub-sampling sizes $\lambda = 32, 64, 128, 256, 512, 4096$. The obtained findings are shown in Fig. 8. It can be seen that when λ is larger than 512, the fault detection performance does not show further considerable improvement with the increase of λ. Thereby, in the further experiments, $\lambda = 512$ and $t = 100$ (number of trees) are used unless specified otherwise.

To demonstrate the superiority of RS-iForest, it is compared to Random Forest (RF), k-Nearest Neighbor method (kNN), and the original iForest[23]. The parameter k determines the number of nearest neighbors, and we set it as $k = 20$ in this experiment. Considering RF, we use $t = 100$ and other parameter values are set to the default ones. In the case of iForest, we set $\lambda = 512$ and $t = 100$. At the same time, to verify the superiority of the copula model based on Gabor wavelets (Copula-Gabor), it is compared to the original Gabor
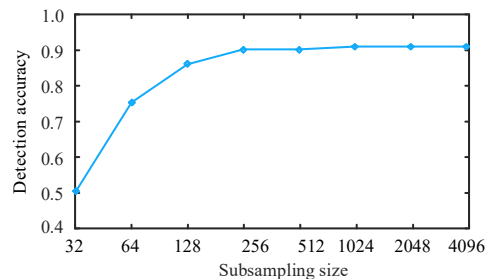

Fig. 8   Correlation between subsampling size and detection accuracy.

texture[13], Bubble Size Distribution[35] (BSD, which has demonstrated a great success in computer vision-aided mineral processing), and velocity distribution[36] (which is also an important observation index for the flotation process control in industry). Figure 9 reports the detection accuracy for all methods in different combinations, and the following observations are obtained: Firstly, compared with other classification methods, RS-iForest consistently achieves the best performance. For example, the average detection accuracy can be improved by 13.3%, 5.6%, and 2.3% compared with kNN, RF, and iForest, respectively. This observation confirms that utilizing rejection sampling to obtain a reasonable ratio between normal and fault instances can further improve the fault detection performance. Secondly, compared with other image features, the Copula-Gabor method can achieve the highest fault detection accuracy.

5.2 Root cause diagnosis

Similarly to the previous section, the performance of the fault root cause diagnosis using TPSR is compared with the alternative methods, such as XGBoost[37], Kernel Partial Least Square (KPLS)[38], and RF. As shown in Fig. 7, the input of these classifiers contains an image feature, feed condition, and reagent dosages. The output of each classifier is the root cause type. In this experiment, three kinds of root causes for each fault type are discussed according to Table 1. Specifically, 400 Fault 1 historic instances and 300 Fault 2 ones are screened by experienced operators. Here, 70% data are randomly divided into training samples, 10% data are used as validation samples, and the remaining 20% data are used as test samples. Table 2 presents the root cause diagnosis accuracy of the aforementioned methods. The obtained result confirms the superiority of TPSR.
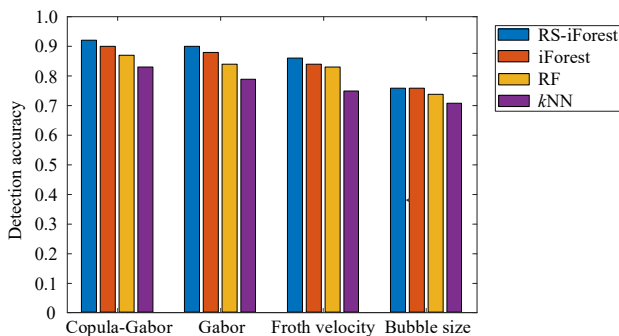

Fig. 9   Comparative analysis on detection accuracy of faulty condition for froth flotation.

Table 2   Comparative analysis on the root cause diagnosis accuracy.

Fault	Root cause	Root cause diagnosis accuracy (%)			
		TPSR	XGBoost	KPLS	RF
Fault 1	Foaming agent	91.2	89.8	84.4	86.3
	Activator	88.9	87.6	78.7	82.8
	Collector	87.7	86.5	77.1	81.9
Fault 2	Foaming agent	92.7	91.3	85.3	87.8
	Activator	90.1	88.3	78.9	84.1
	Collector	88.3	86.6	78.5	83.2

From the experiment results, we can conclude that flotation faults caused by an inappropriate dosage of the foaming agent can be identified easier than other root types. The diagnosis accuracy corresponding to an activator is also higher than that of associated with faults caused by a collector. This result is consistent with the experience of plant operators. In the real industry, a foaming agent is the preferred choice to correct a deviated flotation working condition. If the foaming agent has already been well-controlled, the activator is manipulated to change working conditions. In addition, XGBoost and RF outperform KPLS, and this advantage can be attributed to the ensemble strategies adopted by XGBoost and RF. The difference between XGBoost and RF is significant in this case. The bagging strategy is used in RF, which allows modeling the residual and variance by taking a weighted average of different trees. In its turn, XGBoost trains each subsequent tree using the difference between the predicted values and targets and reduces bias more effectively. Compared with XGBoost, KPLS, and RF, the average accuracy of TPSR was improved by 1.3%, 9.2%, and 5.6% for Fault 1, respectively, and by 1.6%, 9.5%, and 5.4% for Fault 2, respectively. TPSR is constructed from the Sobolev space comprehensively considering both interpolation accuracy and spline smoothness. In a function form, it is defined as a combination of linear and Greens functions providing the greater adaptability to the scattered flotation fault data.

6   Industrial Experiment

The visual perception-based flotation fault detection and diagnosis strategy has been tested and implemented in the largest state lead-zinc flotation plant in China. A computer vision-based flotation process monitoring platform was developed. In this platform, the hardware systems collect the images of a froth surface by using an industrial camera and transmit them to an industrial

computer. The proposed fault detection and diagnosis strategy has been programmed using Microsoft Visual C++ and MAT-LAB and embedded in the industrial computer.

During the two weeks of application, 1008 monitoring events were recorded. The sampling interval was set to 5 min. According to the X-Ray Fluorescence (XRF) analysis results, there were actually 101 Fault 1 events and 53 Fault 2 events summarized in Table 3. The proposed fault diagnosis approach detected 90 Fault 1 events and 48 Fault 2 events. Hence, the average detection accuracy is 89.61%. The verification of the root cause diagnosis is performed through reagent changing. If a direction of a reagent changing, which can facilitate the flotation working condition return to normal, is consistent with the data from Table 1, we consider the fault diagnosis results as appropriate. The average accuracy values corresponding to inferring the root cause for the foaming agent, activator, and collector are 90.70%, 88.64%, and 83.33%, respectively, which demonstrates the high effectiveness of the proposed method.

7 Conclusion

In most of froth flotation plants in China, chemical reagents are changed to control the flotation condition to achieve the designed metallurgical performance. However, performing the chemical reagent control is recognized as a very complex problem, as the kinetic relationships among reagents, inlet air rate, particle size, feed grade, and concentrate grade are still rather unclear. It is inevitable that fault conditions may occur when unreasonable reagents are injected into the flotation bank. To reduce the damage caused by appearing a fault condition and set the production process back to normal working conditions as soon as possible, it is desirable to diagnose faults in a timely manner. In this paper, we presented an intelligent visual perception-based fault

diagnosis approach. It was applied to a process within a lead-zinc flotation plant to diagnose two kinds of faults: when froth is overloaded with mineral particles and when froth lacks mineral particles. It was observed that the proposed framework achieved accurate detection results and demonstrated the high diagnosis performance. As a future research work, we consider combining kinetic mechanisms with intelligent methods to further improve the diagnosis accuracy.

Table 3 Industrial application results. The bold numbers correspond to the actual counts occurred in the experimental period. The numbers that are not in bold correspond to the detection or diagnosis results of the proposed method.

Fault	Faults detection	Number of faults		
		Foaming agent	Activator	Collector
Fault 1	90	56	21	13
	101	**62**	**24**	**15**
Fault 2	48	22	18	7
	53	**24**	**20**	**9**

References

[1] K. X. Peng, K. Zhang, B. You, J. Dong, and Z. D. Wang, A quality-based nonlinear fault diagnosis framework focusing on industrial multimode batch processes, *IEEE Trans. Ind. Electron.*, vol. 63, no. 4, pp. 2615–2624, 2016.

[2] R. Zhang, H. Y. Tao, L. F. Wu, and Y. Guan, Transfer learning with neural networks for bearing fault diagnosis in changing working conditions, *IEEE Access*, vol. 5, pp. 14 347–14 357, 2017.

[3] C. H. Li, W. Zhang, G. L. Peng, and S. H. Liu, Bearing fault diagnosis using fully-connected winner-take-all autoencoder, *IEEE Access*, vol. 6, pp. 6103–6115, 2017.

[4] M. X. Ai, Y. F. Xie, D. G. Xu, W. H. Gui, and C. H. Yang, Data-driven flotation reagent changing evaluation via union distribution analysis of bubble size and shape, *Can. J. Chem. Eng.*, vol. 96, no. 12, pp. 2616–2626, 2018.

[5] P. Tang and T. W. S. Chow, Wireless sensor-networks conditions monitoring and fault diagnosis using neighborhood hidden conditional random field, *IEEE Trans. Ind. Informatics*, vol. 12, no. 3, pp. 933–940, 2016.

[6] D. M. Himmelblau, *Fault Diagnosis and Detection in Chemical and Petrochemical Processes*. Amsterdam, Netherlands: Elsevier, 1978.

[7] I. Hwang, S. Kim, Y. Kim, and C. E. Seah, A survey of fault detection, isolation, and reconfiguration methods, *IEEE Trans. Control Syst. Technol.*, vol. 18, no. 3, pp. 636–653, 2010.

[8] C. H. Xu, W. H. Gui, C. H. Yang, H. Q. Zhu, Y. Q. Lin, and C. Shi, Flotation process fault detection using output PDF of bubble size distribution, *Miner. Eng.*, vol. 26, pp. 5–12, 2012.

[9] M. Lu, W. H. Gui, T. Peng, and W. Cao, Fault condition detection for a copper flotation process based on a wavelet multi-scale binary froth image, *Rem: Rev. Esc. Minas*, vol. 68, no. 2, pp. 177–185, 2015.

[10] G. T. Jemwa and C. Aldrich, Kernel-based fault diagnosis on mineral processing plants, *Miner. Eng.*, vol. 19, no. 11, pp. 1149–1162, 2006.

[11] S. Marcelja, Mathematical description of the responses of simple cortical cells, *J. Opt. Soc. Am*, vol. 70, no. 11, pp. 1297–1300, 1980.

[12] J. G. Daugman, Uncertainty relation for resolution in space, spatial frequency, and orientation optimized by two-dimensional visual cortical filters, *J. Opt. Soc. Am.A*, vol. 2, no. 7, pp. 1160–1169, 1985.

[13] J. Zhang, Z. H. Tang, J. P. Liu, Z. Tan, and P. F. Xu, Recognition of flotation working conditions through froth image statistical modeling for performance monitoring, *Miner. Eng.*, vol. 86, pp. 116–129, 2016.

[14] L. Yu, Z. S. He, and Q. Cao, Gabor texture representation method for face recognition using the Gamma and generalized Gaussian models, *Image Vis. Comput.*, vol. 28, no. 1, pp. 177–187, 2010.

[15] M. N. Do and M. Vetterli, Wavelet-based texture retrieval using generalized Gaussian density and Kullback-Leibler distance, *IEEE Trans. Image Process.*, vol. 11, no. 2, pp. 146–158, 2002.

[16] M. Sklar, Fonctions de répartition à n dimensions et leurs marges, *Publ. Inst. Statist. Univ. Paris*, vol. 8, pp. 229–231, 1959.

[17] N. E. Lasmar and Y. Berthoumieu, Gaussian copula multivariate modeling for texture image retrieval using wavelet transforms, *IEEE Trans. Image Process.*, vol. 23, no. 5, pp. 2246–2261, 2014.

[18] C. R. Li, Y. Y. Huang, and L. H. Zhu, Color texture image retrieval based on Gaussian copula models of Gabor wavelets, *Pattern Recognit.*, vol. 64, pp. 118–129, 2017.

[19] S. Yin, S. X. Ding, X. C. Xie, and H. Luo, A review on basic data-driven approaches for industrial process monitoring, *IEEE Trans. Ind. Electron.*, vol. 61, no. 11, pp. 6418–6428, 2014.

[20] S. Yin, S. X. Ding, A. Haghani, H. Y. Hao, and P. Zhang, A comparison study of basic data-driven fault diagnosis and process monitoring methods on the benchmark Tennessee Eastman process, *J. Process Control*, vol. 22, no. 9, pp. 1567–1581, 2012.

[21] W. H. Li, S. H. Zhang, and S. Rakheja, Feature denoising and nearest–farthest distance preserving projection for machine fault diagnosis, *IEEE Trans. Ind. Informatics*, vol. 12, no. 1, pp. 393–404, 2016.

[22] A. T. Jahromi, M. J. Er, X. Li, and B. S. Lim, Sequential fuzzy clustering based dynamic fuzzy neural network for fault diagnosis and prognosis, *Neurocomputing*, vol. 196, pp. 31–41, 2016.

[23] F. T. Liu, K. M. Ting, and Z. H. Zhou, Isolation forest, presented at the 8th IEEE Int. Conf. Data Mining, Pisa, Italy, 2008.

[24] S. J. Qin, Survey on data-driven industrial process monitoring and diagnosis, *Annu. Rev. Control*, vol. 36, no. 2, pp. 220–234, 2012.

[25] S. M. Xiang, F. P. Nie, C. X. Zhang, and C. S. Zhang, Interactive natural image segmentation via spline regression, *IEEE Trans. Image Process.*, vol. 18, no. 7, pp. 1623–1632, 2009.

[26] S. M. Xiang, F. P. Nie, and C. S. Zhang, Semi-supervised classification via local spline regression, *IEEE Trans. Pattern Anal. Mach. Intell.*, vol. 32, no. 11, pp. 2039–2053, 2010.

[27] J. M. Guo, H. Prasetyo, and K. S. Wong, Vehicle verification using Gabor filter magnitude with gamma distribution modeling, *IEEE Signal Process. Lett.*, vol. 21, no. 5, pp. 600–604, 2014.

[28] A. Sklar, Random variables, joint distribution functions, and copulas, *Kybernetika*, vol. 9, no. 6, pp. 449–460, 1973.

[29] R. Kwitt, P. Meerwald, and A. Uhl, Efficient texture image retrieval using copulas in a bayesian framework, *IEEE Trans. Image Process.*, vol. 20, no. 7, pp. 2063–2077, 2011.

[30] F. T. Liu, K. M. Ting, and Z. H. Zhou, Isolation-based anomaly detection, *ACM Trans. Knowl. Discov. Data*, vol. 6, no. 1, p. 3, 2012.

[31] W. R. Gilks and P. Wild, Adaptive rejection sampling for Gibbs sampling, *J. Roy. Stat. Soc. Ser. C-Appl. Stat.*, vol. 41, no. 2, pp. 337–348, 1992.

[32] A. K. Gupta, *Numerical Methods Using MATLAB*. New York, NY, USA: Apress, 2014.

[33] J. De Andrés, P. Lorca, F. J. de Cos Juez, and F. Sánchez-Lasheras, Bankruptcy forecasting: A hybrid approach using Fuzzy c-means clustering and Multivariate Adaptive Regression Splines (MARS), *Expert Syst. Appl.*, vol. 38, no. 3, pp. 1866–1875, 2011.

[34] J. Zhang, Z. H. Tang, W. H. Gui, Q. Chen, and J. P. Liu, Interactive image segmentation with a regression based ensemble learning paradigm, *Front. Inform. Technol. Electron. Eng.*, vol. 18, no. 7, pp. 1002–1020, 2017.

[35] J. Zhang, Z. H. Tang, M. X. Ai, and W. H. Gui, Nonlinear modeling of the relationship between reagent dosage and flotation froth surface image by Hammerstein-Wiener model, *Miner. Eng.*, vol. 120, pp. 19–28, 2018.

[36] J. Zhang, Z. H. Tang, M. X. Ai, and W. H. Gui, Fuzzy association rule based froth surface behavior control in zinc froth flotation, *Symmetry*, vol. 10, no. 6, p. 216, 2018.

[37] T. Q. Chen and C. Guestrin, XGBoost: A scalable tree boosting system, presented at the 22nd ACM SIGKDD Int. Conf. Knowledge Discovery and Data Mining, San Francisco, CA, USA, 2016.

[38] Y. W. Zhang and C. Ma, Fault diagnosis of nonlinear processes using multiscale KPCA and multiscale KPLS, *Chem. Eng. Sci.*, vol. 66, no. 1, pp. 64–72, 2011.

Jin Zhang received the master's degree in software engineering from the Central South University, Changsha, China in 2016, where he is currently pursuing the PhD degree. His research interests include computer vision, deep learning, and process monitoring and control.

Zhaohui Tang received the bachelor's degree from Central South University in 1988. He received the MS and PhD degrees in control science and engineering from Central South University, Changsha, China in 1997 and 2008, respectively. During October 2005–September 2006, as a visiting scholar, he had been carrying out the cooperative research on the complex control and fault diagnosis technology at the Institute of Complex Control, Duisburg-Essen University in Germany. He is currently a full professor at the School of Automation, Central South University. His main research interests include modeling and optimal control of the complex industrial system, fault diagnosis, the research and application of computer control system, and image processing technology.

Yongfang Xie received the BS, MS, and PhD degrees in control science and engineering from Central South University, Changsha, China in 1993, 1996, and 1999, respectively. From 1999 to 2003, he was with the Tokyo International Information Science Research Institute, Tokyo, Japan and also a visiting scholar at the PToPA Research Institute, Tokyo. He is currently a full professor at the School of Automation, Central South University. His current research interests include modeling, optimization, and control of complicated industrial processes, distributed robust control, and fault diagnoses.

Mingxi Ai received the master's degree in aeronautical and astronautical science and technology from Central South University, Changsha, China in 2016, where she is currently pursuing the PhD degree. Her research interests include image processing, machine learning, modeling, and control of complicated industrial processes.

Weihua Gui received the BS and MS degrees from Central South University, Changsha, China in 1976 and 1981, respectively. He was a visiting scholar at the Universität GH Duisburg, Duisburg, Germany from 1986 to 1988. Since 1991, he has been a full professor at Central South University. Since 2013, he has been an academician at Chinese Academy of Engineering. His current research interests include modeling and optimal control of complex industrial processes, distributed robust control, and fault diagnoses.